We are IntechOpen, the world's leading publisher of Open Access books Built by scientists, for scientists

4,800
Open access books available

122,000
International authors and editors

135M
Downloads

Our authors are among the

154
Countries delivered to

TOP 1%
most cited scientists

12.2%
Contributors from top 500 universities

CLARIVATE ANALYTICS BOOK CITATION INDEX INDEXED

WEB OF SCIENCE™

Selection of our books indexed in the Book Citation Index in Web of Science™ Core Collection (BKCI)

Interested in publishing with us?
Contact book.department@intechopen.com

Numbers displayed above are based on latest data collected.
For more information visit www.intechopen.com

9

Carotid Plaque Stresses

Samuel Alberg Kock[1] and Jens Vinge Nygaard[2]
[1]*Aarhus University Hospital Skejby,* [2]*Aarhus University: iNANO*
Denmark

1. Introduction

Cardiovascular atherosclerotic disease is the leading cause of death and severe disability worldwide (Rosamond et al., 2007; WHO and CDC, 2004; Yusuf et al., 2001). Carotid atherosclerotic plaques are a major cause of cerebrovascular thromboembolic events including transitory ischemic attacks and strokes (Virmani et al., 2006; Redgrave et al., 2006; Nighoghossian et al., 2005; Carr et al., 1996).

1.1 Current Carotid Risk Assessment

In current clinical practice, selection for surgical removal of the carotid plaque (carotid endarterectomy) is determined by the degree of luminal narrowing known as the degree of stenosis (Rothwell et al., 2003a). The operation has been determined beneficial in patients with symptomatic, severe stenosis in two large, randomized trials; the North American Symptomatic Carotis Endarterectomy Trial (NASCET, 1991) and the European Carotid Surgery Trial (ECST, 1998). To determine the degree of stenosis, NASCET and ECST used measurements based on x-ray digital subtraction angiographies. Today, Doppler ultrasound is used in clinical practice for determination of the degree of stenosis (Nederkoorn et al., 2003; Titi et al., 2007). This technique does not rely on direct measurements of the degree of stenosis but uses determination of maximum peak systolic and end diastolic blood flow velocities as well as the spectral composition of these velocities to assess the degree of stenosis. The ultrasound Doppler techniques, though in universal clinical use, are problematic due to problems with the insonation angle affecting the Doppler equation (Tola and Yurdakul, 2006; Claudon et al., 2001), inter- and intra-observer variations (Mead et al., 2000; Lui et al., 2005), and interpretation in the presence of complex geometries (Clevert et al., 2006; Clevert et al., 2007).

Preventive treatment of patients with carotid plaques but no symptoms (asymptomatic patients) would be preferable but is controversial, since trials have shown only marginal effect of treatment from current risk stratification, and total mortality after five years is unchanged in treated vs. untreated groups (Halliday et al., 2004; Redgrave et al., 2006). To prevent a single stroke, the number needed to treat for symptomatic patients is seven (Rothwell et al., 2003a) rising to forty for asymptomatic patients (Halliday et al., 2004).

Using the current risk assessment algorithm, the majority of patients operated are thus needlessly exposed to peri-operative risks. Further, atherosclerotic plaques tend to grow outwards initially, which may result in normal luminal size belying substantial plaque volumes, a process known as arterial remodeling (Glagov et al., 1987; Glagov et al., 1988;

Pasterkamp and Smits, 2002) making risk assessment based on the degree of stenosis problematic. In addition, most ruptured plaques are less than 50% stenosed, the current limit at which carotid endarterectomy is offered (Casscells et al., 2003; Falk et al., 1995).
Thus, the decision of whether or not to operate is based on scientifically problematic methodologies. A great need therefore exists for improved methods of selecting patients with carotid atherosclerosis who may benefit from operation.

1.2 Vulnerable Plaque Features

Histological examinations have determined the hallmarks of plaques at risk of rupture (vulnerable plaques) to be large lipid-rich, necrotic cores covered with thin fibrous caps (Virmani et al., 2006; Gronholdt et al., 1998; Falk, 2006; Naghavi et al., 2003; Casscells et al., 2003; Virmani et al., 2000; Stary et al., 1995). Many studies have shown that inflammation and the subsequent immune response contribute to atherosclerosis. Further, blood pressure is known to influence the incidence of strokes (Kario et al., 2003; Staessen et al., 1997; Dart and Kingwell, 2001; Rothwell et al., 2003b).

1.3 Plaque Imaging

Through the advent of high-resolution in-vivo imaging techniques such as intravascular ultrasound (Sipahi et al., 2007; Imoto et al., 2005), optical coherence tomography (Huang et al., 1991; Yabushita et al., 2002), and magnetic resonance imaging (MRI) (Yuan and Kerwin, 2004), detailed morphologic and structural characterization of atherosclerotic plaques has been enabled. In particular, MRI has proven a valuable modality for imaging carotid plaques with the capability of non-invasively imaging necrotic cores (Yuan et al., 1997; Yuan et al., 2001), fibrous caps (Hatsukami et al., 2000; Yuan et al., 2002; Mitsumori et al., 2003), and presence of intraplaque hemorrhage (Chu et al., 2004). Indeed, the characterization of atherosclerotic lesions using MRI approaches histological definitions (Cai et al., 2002). Recently, semi-automated tissue segmentation has been enabled (Liu et al., 2006). Furthermore, MRI has the ability to measure blood velocities through phase-contrast imaging (Firmin et al., 1990; McDonnell, III et al., 1994) and deformations using cine MR imaging (Draney et al., 2002; Metafratzi et al., 2002).

1.4 Computational Simulations of Plaque Stresses

Since plaque rupture by definition represents a structural failure of the protective fibrous cap, it seems reasonable to assume that plaque morphology as well as biomechanical properties of the atherosclerotic lesion may influence the plaque vulnerability. To estimate stress levels in the fibrous cap, fluid structure interaction analysis has emerged as a tool combining blood flow simulation through computational fluid dynamics combined with finite element analysis of the corresponding stress levels in the surrounding tissues. Thus, a number of studies have been performed investigating intraplaque stresses as a potential risk marker of vulnerable plaques (Li et al., 2006a; Imoto et al., 2005; Kaazempur-Mofrad et al., 2004; Chau et al., 2004; Steinman, 2002; Huang et al., 2001; Li et al., 2006b; Tang et al., 2004; Zhao et al., 2002). Indeed, in vitro studies of coronary arteries have shown markedly elevated fibrous cap stresses in ruptured coronary lesions compared to stable lesions (Cheng et al., 1993) and a recent publication found carotid fibrous cap stress levels in symptomatic patients to be nearly twice those of asymptomatic patients (Li et al., 2007).

In principle, 3D simulations of fibrous cap stresses would be preferable since they inherently provide more information than 2D sections. However, the computational demands for performing 3D fluid structure interaction simulations are great requiring substantial solution times. Thus, simulations in 2D cross-sections corresponding to either histological data (Cheng et al., 1993) or MRI scans (Li et al., 2006a) have been suggested. Though the use of cross-sectional data matches the orientation of the available morphologic data, this approach precludes fluid structure interaction analysis and necessitate assumptions regarding the longitudinal blood pressure distribution used to load the blood/vessel wall interface. We have recently developed a novel semi-automated method of creating longitudinal 2D models from transverse MRI scans allowing simulations of longitudinal stress distributions including the effects of fluid structure interactions and determination of correct blood pressure distribution enabling predictions of plaque rupture risk and examinations of correlations between local stress variation and morphology.
To investigate the clinical usefulness of the method, we performed fluid-structure interaction simulations of an idealized carotid artery based on the geometry of a symptomatic patient. We investigated the impact of different known markers of plaque vulnerability, i.e. propensity for rupture, namely degrees of luminal stenosis, fibrous cap thicknesses, lipid core sizes, and lipid core positions to determine their effect on plaque stress levels and risk of plaque rupture.

2. Morphology Generation

A variety of imaging modalities have been employed for generating morphology suitable for computational fluid dynamics simulations including magnetic resonance imaging (Li et al., 2006a; Tang et al., 2004), intravascular ultrasound (Wentzel et al., 2003; Ramaswamy et al., 2006), computed tomography (Jin et al., 2004), and optical coherence tomography (Chau et al., 2004). In particular, magnetic resonance imaging has gained widespread usage as the method-of-choice for producing computational fluid dynamic models given the modality's excellent soft tissue contrast and inherent capability of obtaining velocity images alongside the morphological imagery. In addition, dynamic deformational images may be obtained allowing for evaluations of the computational simulations with regards to induced deformations. In the present work, magnetic resonance imaging was used to scan a a male patient (age 69) with a 70% stenosed carotid artery, awaiting surgery for carotid atherosclerosis who gave informed written consent before participation. The protocol was approved by the local ethics committee.

2.1 Plaque Morphology

The critical plaque components to be identified include lipid-rich necrotic cores, fibrous caps, and intraplaque hemorrhages. Histological studies have demonstrated that plaque tissue components often exist in a mixture state, especially in advanced lesions. Thus lipid-rich necrotic cores largely consist of cholesterol esters, free cholesterols, and triglycerides, which all contribute differently to the MRI signal based on their physical states (Yuan et al., 2001; Small and Shipley, 1974). In addition, signal features of intraplaque hemorrhage may change depending on the evolution stage (Chu et al., 2004). A single contrast weighting is thus insufficient for characterizing plaque tissues. Therefore, noninvasive visualizations of

carotid plaque morphology mainly rely on multispectral (or multicontrast) weighted MRI techniques to characterize atherosclerotic lesions.

A well-validated MRI multicontrast protocol has been developed for the noninvasive detection and characterization of atherosclerotic plaques in carotid arteries employing T1-weighted (T1W), T2-Weighted (T2W), Proton Density Weighted (PDW), and Time Of Flight (TOF) scans (fig. 1) (Yarnykh and Yuan, 2003; Yuan and Kerwin, 2004; Cai et al., 2002).

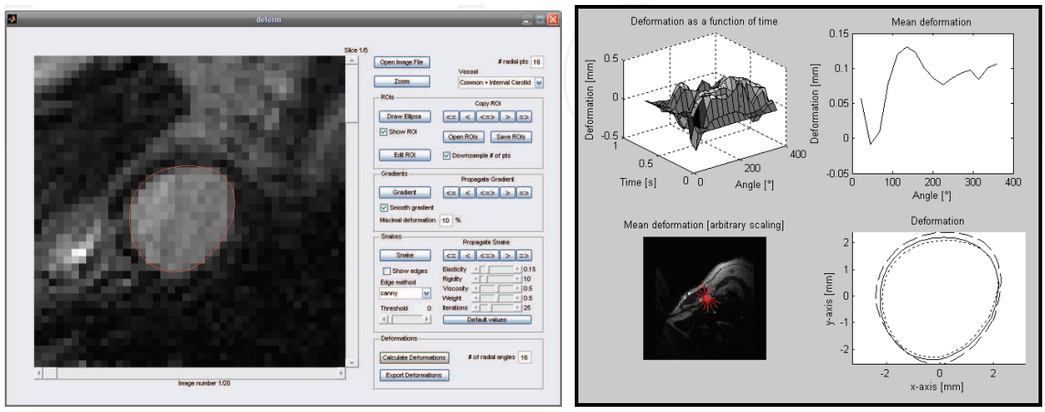

A B

Figure 1. Custom Matlab toolbox for measuring time-resolved deformation. A: Cross-sectional B-TFE MRI scan with contour of CCA outlined in red. B: Top left: Deformation as a function of time and radial angle. Top right: mean deformation as a function of radial angle. Bottom left: Mean radial deformation overlaid the MRI scan. Bottom right: Mean (solid line), maximal (dashed line), and minimal (dotted line) deformation

Though current state of the art MRI protocols for carotid plaque imaging have an accuracy proven to approach histological AHA classifications of plaque morphology (Cai et al., 2002), current spatial resolution of the employed sequences is only 0.6x0.6x2 mm. The critical fibrous cap thickness is typically thought to be below 0.25 mm in the carotid artery, and below 0.1 mm in the coronaries (Bassiouny et al., 1997; Li et al., 2006b; Imoto et al., 2005). Increasing spatial resolution of MRI scans to enable visualization of very thin fibrous caps of 0.25 mm or below in thickness could thus prove of importance. Moving towards scanners with higher field strengths (Yarnykh et al., 2006) or switching from 2D to 3D acquisitions (Koktzoglou and Li, 2007) may facilitate this.

Presently, complete morphological imaging of the carotids requires scans with a total duration of approximately 45 minutes. Though shortened scan times would be desirable in terms of clinical feasibility, signal-to-noise ratios will thereby be negatively impacted. The conflicting demands of time requirements and signal-to-noise ratio must be considered, and compromises reached. The increased signal-to-noise ratio of scanners with higher field strengths and 3D acquisitions may also be used for shorter scan durations instead of increased resolution.

The carotid arteries are superficial structures whose length is greater than their distance from the surface, a configuration well suited for the use of phased-array coils consisting of several adjacent small surface coils from which data are collected simultaneously (Hayes et al., 1996; Botnar et al., 2001; Roemer et al., 1990). Such coils have been reported to increase signal-to-noise ratio by 37% and would be preferable for carotid imaging (Yuan and Kerwin, 2004).

2.2 Velocity Measurements

Phase-contrast MRI scans may be used to measure time-resolved blood velocities in the internal (ICA), external (ECA), and common (CCA) carotid arteries over a cardiac cycle. The accuracy of phase-contrast MRI is generally considered high, even in unsteady flows as present in patients with severe degrees of stenosis (Frayne et al., 1995).

The measured velocities were applied at the ICA and ECA as parabolic flow profiles. Previous studies have shown non-parabolic velocity profiles in the carotid arteries affecting the WSS distributions (Perktold and Rappitsch, 1995). However, since stress levels are mainly the result of pressure distributions rather than effects of blood flow adjacent to the vessel walls, these are thought to be less affected thereby.

2.3 Vessel Deformation

Vessel deformation can be monitored using a cine MRI Balanced True Field Echo sequence (B-TFE). A custom Matlab toolbox (fig. 1) was constructed allowing semi-automatically measurements of deformations as a function of time and radial position. An initial circle surrounding the carotid vessel was drawn, the center of mass found, and a polar image constructed of the carotid vessel. Using thresholding, the vessel outline was detected and transformed back to a Cartesian space. Snakes were used to generate smooth outlines surrounding the vessel (Yuan et al., 1999).

The measured deformations can be used for tuning material parameters of the tissue surrounding the carotids to ensure deformations in the computational simulations matches the in-vivo measurements.

2.4 Segmentation

As previously stated, atherosclerotic tissues may exhibit heterogeneous signal levels necessitating the use of multicontrast protocols. Table displays the appearance of typical plaque features on the different contrast weightings. Given this heterogeneity, reproducibility of the segmentations might have been expected to be low. However, the opposite holds true, studies have shown excellent reproducibility of MRI-based segmentations of carotid plaque morphological features.(Yuan et al., 1998; Shinnar et al., 1999) Further, all the scans presented in I, II, and III were validated by an experienced reviewer at the Vascular Imaging Lab at the University of Washington, USA. Recently, an approach utilizing computational morphology enhanced probability maps was described allowing for fully automated segmentation of carotid plaque morphology.(Liu et al., 2006)

Plaque Component	MR Contrast Weighting			
	TOF	T1W	PDW	T2W
Recent intraplaque hemorrhage	+	+/0	-/0	-/0
lipid-rich necrotic cores	0	+	-/0	-/0
Intimal calcifications	-	-	-	-

Table 1. Magnetic resonance imaging criteria used to identify plaque tissue components (Yuan et al., 2001). The intensities listed are relative to the adjacent sternocleidomastoid muscle

2.5 Computational Model Generation

The segmented data describing the spatial distribution of plaque components in each MRI slice were exported as a collection of spline curves. These were imported into Matlab® R2006b (The MathWorks Inc., Natick, MA, USA) and converted to 2D grayscale images (fig. 2). From the 2D images, a region-of-interest was selected and collected into a single 3D matrix describing the spatial distribution of segmented tissue within the scanned volume. The dataset was resampled using linear interpolation to obtain an isotropic voxel size of 0.3125x0.3125x0.3125 mm^3 followed by Gaussian smoothing.

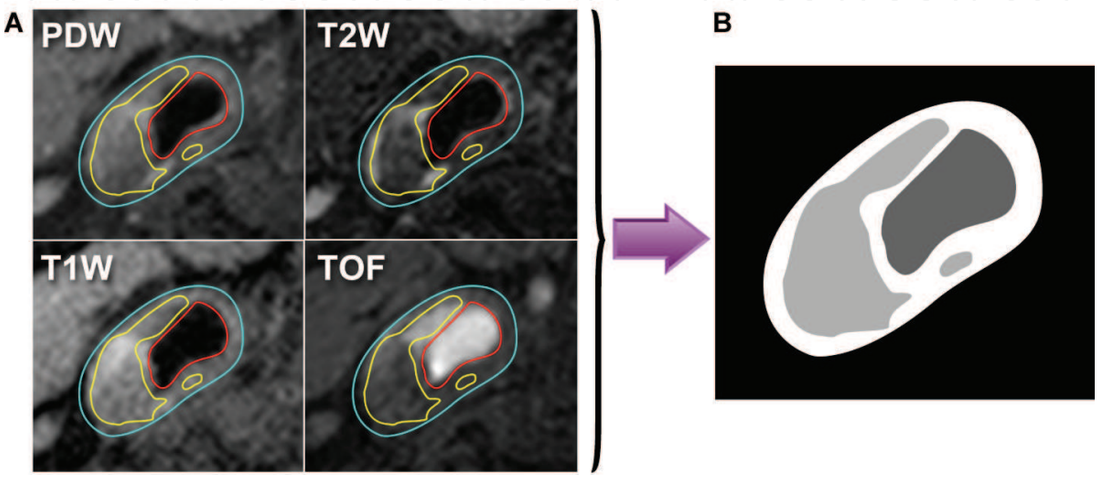

Figure 2. (A) Four MRI weightings were performed in order to enable segmentation into blood, vessel wall, and lipid-rich necrotic core. PDW=Proton Density Weighted image, T2W=T2 Weighted image, T1W=T1 Weighted image, TOF=Time Of Flight scan. (B) Grey-scale images were constructed from the segmented MRI images and used for constructing logical images oft he plaque morphological distribution. Visible features include blood stream (red), vessel wall (purple), and lipid-rich necrotic cores (yellow)

From the isotropic dataset, isosurfaces surrounding each component were created (fig. 3A). To create a longitudinal 2D model, the 3D isosurface model was sectioned along skeletonization points by a Non-Uniform Rational B-Spline (NURBS) (Piegl and Tiller, 1997) surface (fig. 3A), yielding a final 2D model to be analyzed (fig. 3B). To minimize boundary effects the model was extended linearly 5 cm up- and downstream, corresponding to approximately five times the CCA diameter.

The close proximity of blood lumen and lipid-rich necrotic cores, with fibrous cap thicknesses of 0.25 mm or below may cause problems with overlapping isosurfaces in some patients, necessitating manual adjustment of interpolation and smoothing parameters. Further, due to the slice thicknesses of 2 mm employed in the MRI scans, the flow divider was seldom depicted and the resulting longitudinal model had a distinct flattened profile at this location. Thus manual adjustment of the area surrounding the flow divider from longitudinal MRI scans was needed.

Initially, the patient was scanned using the aforementioned magnetic resonance protocol which was used to generate an initial model using the described methodology. In order to suppress local effects of uneven vessel wall borders, a simplified longitudinal model was created using the previously generated curves as guidelines. A cosine function was used to

generate the walls surrounding the plaque, initially calculated horizontally before being rotated using the plaque angle (-65.5°).

$$f(x) = \left(\frac{S * MS}{100} - mS\right) * \left(\frac{1}{2} + \frac{1}{2} * \left(\cos\left(\frac{2\pi}{l} * x - \pi\right)\right)\right) \quad (1)$$

where f = horizontal plaque height, S = degree of stenosis in percent, MS = amplitude at 100% degree of stenosis, mS = amplitude at 0% degree of stenosis (negative), and l = length of stenosis. User-selected amplitudes (S) were applied to simulate models with 95%, 90%, 80%, and 70% degrees of stenosis, measured using the NASCET standard (Rothwell et al., 2003a). Lipid pools were generated as ellipsoids with varying sizes (6x3 mm, 4x2 mm, and 2x1 mm) inside the plaque area at specified locations to generate models with proximal/distal lipid core position and decreasing fibrous cap thicknesses (0.5, 0.2, 0.1, and 0.05 mm).

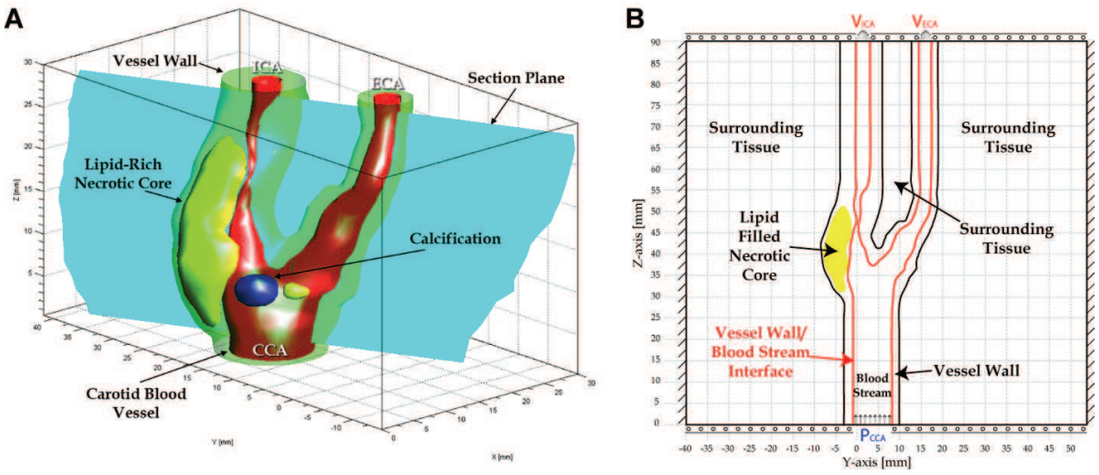

Figure 3. (A) A 3D skeletonization was performed on the blood-stream and a NURBS surface constructed intersecting the center of the blood stream throughout the model. (B) Intersections between NURBS surface and the iso-surfaces delineating the plaque tissues were used to derive a longitudinal 2D model which was embedded in a slab of surrounding tissue. External boundary conditions are also presented, rollers at top and bottom with fixed boundaries at either side. ICA = Internal Carotid Artery, ECA = External Carotid Artery, CCA = Common Carotid Artery, V_{ICA} = Velocity at ICA, V_{ECA} = Velocity at ECA, P_{CCA} = Pressure at CCA

2.6 Boundary Specifications

Blood flow was simulated as Navier-Stokes flow and treated as an incompressible, homogeneous, Newtonian, viscous fluid with a density of 1050 kg/m^3 and dynamic viscosity of 0.0035 Pa·s. The two outflows were specified as parabolic velocity outlets using the phase-contrast MRI measured mean blood flow velocities of the patient at the internal and external carotids (fig. 3B). A no-slip boundary condition was applied along the blood-stream/vessel wall interface, and an Arbitrary Lagrangian-Eulerian (ALE) formulation was used to couple the fluid forces to the structural deformation and vice versa along the vessel wall/blood-stream interface. Reynold's number in the normal healthy carotid is insufficient

to warrant turbulence modeling, however flow fields in carotid phantoms with large degrees of stenosis are more accurately depicted using κ-ω models than both laminar flow and κ-ε turbulence models (Banks and Bressloff, 2007). If blood flow is modeled as being turbulent, recent research suggests that the κ-ω model is superior with regard to flow field depiction (Banks and Bressloff, 2007), thus this model was chosen.

A carotid pulse pressure profile was measured noninvasively using the applanation tonometry technique (Chen et al., 1996; Zhao et al., 2002) with a high-fidelity external pressure transducer (SPT-301, Millar Instruments Inc., Texas, USA) applied to the skin above the common carotid artery. The pulse pressure profile was scaled using the systolic and diastolic blood pressures of the patient and applied as the inlet boundary condition at the common carotid inlet.

The model was embedded in a rectangle of surrounding tissue the width of which was determined from cross-sectional MRI scans. Left and right boundaries were fully constrained and top and bottom boundaries (excluding the fluid boundaries) constrained in the Z-direction. The boundary between the top surrounding tissue block and vessel wall was also fully constrained (fig. 3B).

Using MRI phase contrast scans, fluid velocities were measured at both outlets in the patient with 70% degree of stenosis. To account for the change in velocities caused by the varying degree of stenosis, the internal carotid artery was modeled as a Venturi tube:

$$Q = C \cdot \sqrt{\frac{1}{1-(D_2/D_1)^4}} \cdot \frac{\pi \cdot D_2^2}{4} \cdot \sqrt{\frac{2 \cdot \Delta p}{\rho}} \tag{2}$$

where Q = volumetric flow rate, C = coefficient of discharge (0.77), D_1 = diameter of normal internal carotid artery (after the stenosis), D_2 = diameter of internal carotid artery at maximal point of constriction, Δp = pressure difference, and ρ = mass density of blood (1050 kg/m^3).

Initial conditions were specified using the diameters and flow measured in the patient to estimate the pressure difference. Subsequently, the D_2 diameter was changed to that of the individual degrees of stenosis, and the resulting flows (Q) were used to calculate the velocities in the internal carotid artery in each of the models. To preserve common carotid flow rate, the loss in internal carotid flow was assigned to the external carotid. Laminar, parabolic velocity profiles were assigned at both outlets using the calculated velocities. The systolic blood pressure of the patient was prescribed at the inlet (160 mmHg ≈ 21.300 Pa). The blood was initialized using the inlet blood pressure and mean external outlet velocity. Although a simplification, blood was simulated as a Newtonian fluid with a constant viscosity. Due to the content of formed elements within the bloodstream shear thinning occurs in vivo and the viscosity is not constant. However, recent research (Lee and Steinman, 2007) suggests that the use of Newtonian models for simulations of blood flow are reasonable in the carotid artery.

2.7 Material Properties

Tissues were simulated as isotropic homogenous entities. To account for the non-linear stress/strain dependency of human tissues, a computationally efficient Neo-Hookean hyper-elastic model was used to specify the material properties of the tissues using the following strain energy function (W):

$$W = \frac{\mu}{2} \cdot (\bar{I}_1 - 3) + \frac{K}{2} \cdot (J - 1)^2 \quad (3)$$

where μ designate the initial shear modulus and $\bar{I}_1$ is the first deviatoric strain invariant, J is the ratio of the deformed elastic volume over the undeformed volume, and K is the bulk modulus calculated as follows:

$$K = \frac{2 \cdot (C_1 + C_2)}{1 - 2 \cdot \nu} \quad (4)$$

where C_1 and C_2 are the material constants in the Mooney-Rivlin hyper-elastic model (the Neo-Hookean model can be considered a subset of the Mooney-Rivlin model with $C_1 = 0$ and $C_2 = \mu / 2$), ν represents Poisson's ratio, assigned to be *0.495* to mimic the almost incompressible human tissues. The initial bulk modulus K was thus set to *100* times that of the initial shear modulus. The initial shear modulus μ was set to 6 MPa for the vessel wall (COMSOL AB, 2005). Lipid was treated as an isotropic material with Young's modulus set to 1/100th that of the equivalent Young's modulus of the vessel wall (Young's modulus = 1E5 Pa, Poisson's ratio = 0.45) (Tang et al., 2004). The initial shear modulus of the surrounding tissue was adjusted until the deformation near the common carotid inlet matched that measured by MRI B-TFE scans as measured by the change in vessel diameter between diastole and systole.

The Neo-Hookean model is considered to be valid for the moderate deformations present in atherosclerotic plaques and was validated with a geometry similar to a previously described model (Li et al., 2006b). Other researchers have used linear orthotropic models (Imoto et al., 2005), modified Mooney-Rivlin models (Chau et al., 2004; Tang et al., 2004), and Ogden hyperelastic models (Li et al., 2007; Versluis et al., 2006; Antheunis et al., 2006). Since different hyperelastic models and material specifications may substantially affect resulting stress levels, comparison of stress levels between different models should be interpreted with caution.

To simplify the present finite element analysis, the materials were assumed to be isotropic, incompressible, and uniform solids. By assuming that plaques, lipids, and normal arterial walls could each be characterized by a single set of structural variables, spatial and interspecimen variations within a particular component were not considered (Holzapfel et al., 2004). However, these assumptions have been widely accepted as allowable for the assessment of biomechanical properties of atherosclerotic lesions (Loree et al., 1992; Cheng et al., 1993; Imoto et al., 2005).

2.8 Solving the FSI model

The coupled fluid–structure interaction simulations were performed using COMSOL, a commercially available finite element solver (COMSOL 3.4, COMSOL Inc, Stockholm, Sweden). Streamline diffusion was applied to artificially stabilize the solution.

3. Results

Two examples of velocity fields, first principal stress distributions, and velocity streamlines are presented in fig. 4. A 90% degree of stenosis model with a proximal 6x3 mm lipid core and minimal fibrous cap thickness of 0.2 mm yielded maximal principal stresses of 674.4 kPa occurring at the area of minimal fibrous cap thickness (fig. 4A, red arrowhead). Immediately

adjacent to the area with maximal first principal stresses equal to tensile stresses, was a pressure zone with negative first principal stresses of -101.4 kPa (fig. 4A, white arrowhead). A second model with 80% degree of stenosis, a distal 4x2 mm lipid core, and minimal fibrous cap thickness of 0.2 mm is presented in fig. 4B. The velocities in the internal carotid artery were higher in this model due to the Venturi calculations, generating a large zone of recirculating blood above the plaque (fig. 4B, yellow asterisk). Again, maximal (fig. 4B, red arrowhead) and minimal (fig. 4B, white arrowhead) first principal stresses were found to be adjacent and located at the area of minimal fibrous cap width, with a magnitude of 429.1/-89.5 kPa, respectively.

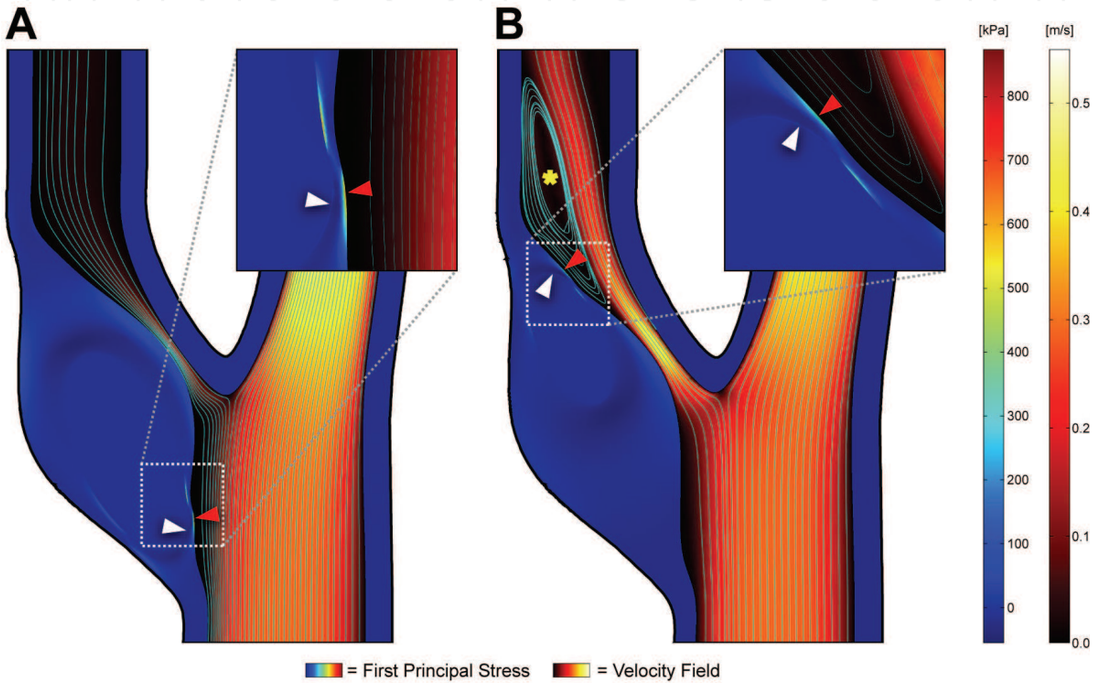

Figure 4. Examples of the results generated from the simulations. Arrowheads mark the location of maximal/minimal first principal stresses, red/white respectively. Insets depicts areas of maximal/minimal stress levels. (A) Carotid with 90% stenosis, proximal 6x3 mm lipid pool, and minimal fibrous cap width of 0.2 mm. (B) Carotid with 80% stenosis, distal 4x2 mm lipid pool, and minimal fibrous cap width of 0.2 mm. A large zone of recirculating blood was present above the plaque (yellow asterisk)

The combined effects of degrees of stenosis, fibrous cap thicknesses, lipid core size, and lipid core location on peak principal stress levels are depicted in fig. 5. Stresses are seen to increase with decreasing fibrous cap thickness, and increasing degrees of stenosis. However, the degree of stenosis mainly affects peak principal stresses in models with fibrous caps below 0.2 mm in width. This is evident by the observation that the variation in peak principal stresses increases as the fibrous cap width decreases. Lipid core sizes have a marked influence on peak principal stress levels. Peak principal stress in a model with 95% degree of stenosis, a proximal lipid core, and fibrous cap thickness of 0.1 mm varied from 1861.2 kPa with a 6x3 mm lipid core to 445.6 kPa with a 2x1 mm lipid core.

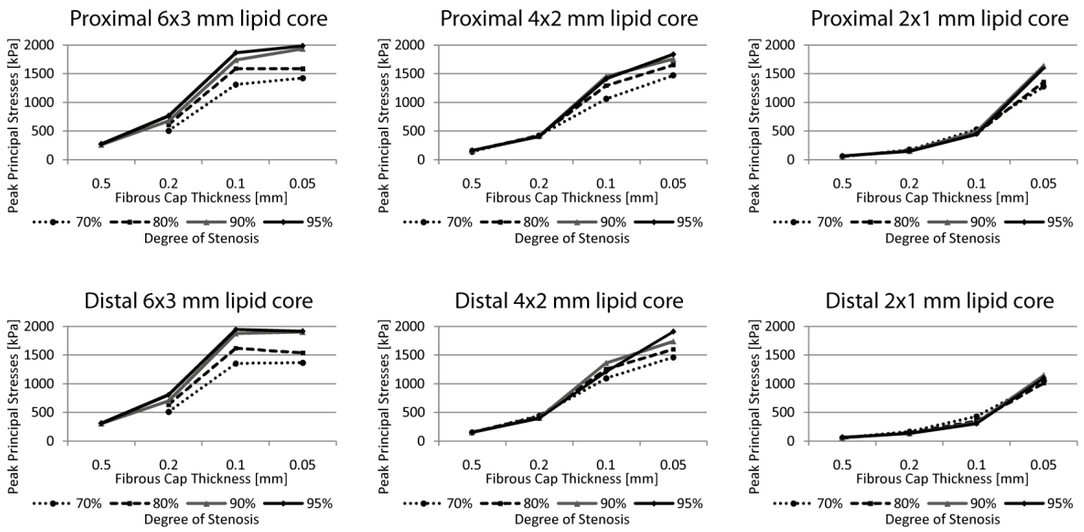

Figure 5. Effects of fibrous cap thickness, degree of stenosis, lipid core size, and lipid core position on peak principal stress levels

The longitudinal position of the lipid core did not affect peak principal stress levels in this model, as shown in fig. 5. Also evident in fig. 5 are the effects of decreasing lipid core sizes producing substantial reductions in median peak principal stress levels.

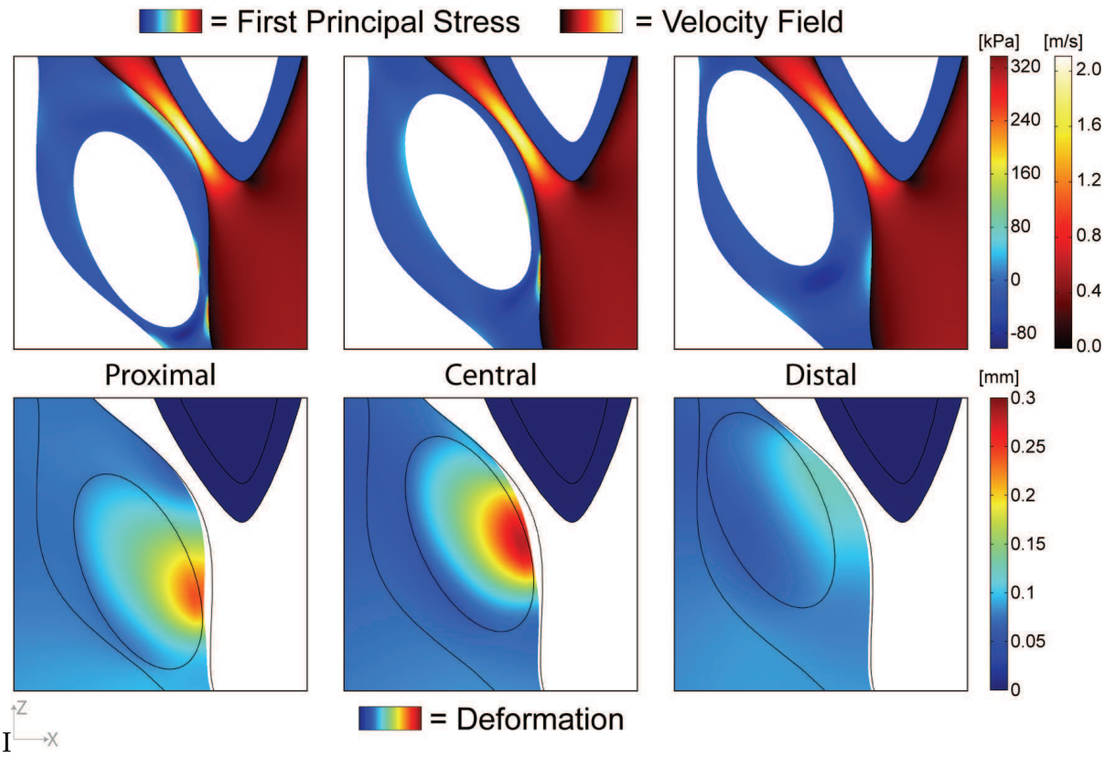

Figure 6. Principal stress levels and deformations as a function of lipid core position in a model with 90% degree of stenosis, 0.5 mm fibrous cap thickness, and 6x3 mm lipid core size

n another model with a 90% degree of stenosis employing the original flow values measured in the patient with a 70% degree of stenosis instead of using the Venturi calculations, lipid core position was seen to influence peak principal stress levels substantially, as presented in fig. 6. Using this model, peak principal stresses were 323.4 kPa, 335.0 kPa, and 64.6 kPa in the proximal, central, and distal lipid core simulation, respectively.

4. Discussion

Currently, carotid risk assessment is based on measuring the degree of stenosis to determine if carotid endarterectomy should be offered symptomatic patients (NASCET, 1991; ECST, 1991; Rothwell et al., 2003a). However, there is growing evidence that morphological composition rather than degree of luminal stenosis may be the deciding factor in determining plaque vulnerability (Virmani et al., 2006; Gronholdt et al., 1998; Falk, 1992). In particular, large lipid cores with thin fibrous caps have been determined to be the hallmark of unstable plaques at high risk of rupture. Through the advent of high-resolution MR imaging combined with computational analysis, in-vivo estimations of mechanical stresses in the fibrous cap have been enabled (Li et al., 2007; Tang et al., 2004; Zhao et al., 2002).

In a recent study by Li et al. (Li et al., 2006b), the effect of stenosis severity and fibrous cap thickness on resulting mechanical stress levels was investigated. This study showed that plaques with a degree of stenosis at 70% or above all gave rise to high fibrous cap stress levels regardless of fibrous cap width. Plaques with lower degrees of stenosis also reached high stress levels depending on the thickness of the fibrous cap. However, to simplify the computational analysis a straight tube without bifurcation was used and the plaque was modeled as a large homogeneous lipid core covered by a fibrous cap of varying thickness.

In our study, we used an idealized bifurcation model based on geometry obtained from a patient awaiting carotid endarterectomy. Ellipsoidally shaped lipid cores were used to create heterogeneous plaques with varying position of the lipid cores allowing for examinations of the effects of lipid core size and position in addition to the effects of the degree of stenosis and fibrous cap width. To account for the effect of increasing degrees of stenosis on fluid flows, the internal carotid artery was modeled as a Venturi tube, and the velocities adjusted accordingly.

The findings of Li et al. (Li et al., 2006b) were confirmed; increasing degrees of stenosis and decreasing fibrous cap thicknesses were found to affect peak principal stress levels severely (fig. 5). Though decreases in fibrous cap width was by far the most influential parameter on fibrous cap stress levels it cannot stand alone. Lipid core sizes also impacted mechanical stress levels significantly (fig. 5) and a comprehensive approach towards fibrous cap mechanical stress estimations is deemed important.

In an angiographic study of plaque ulceration, Lovett (Lovett and Rothwell, 2003) determined ulcerations to be asymmetrically distributed longitudinally with the majority occurring upstream to the plaque rather than downstream. To investigate if this phenomenon could be attributed to mechanical stress levels, symmetrical simulations were performed with lipid cores placed proximally and distally inside the plaque. However, no significant differences were found between models with proximal cores vs. distal cores, indeed the stress levels were virtually identical except for very small lipid cores (fig. 5). This effect may be due to the modeling of the internal carotid artery as a Venturi tube keeping the pressure difference across the stenosis constant. Thus a second round of simulations was performed using the original flow values measured in the patient with a 70% degree of

stenosis instead of adjusting these using the Venturi calculations. These revealed vast increases in stress levels if the fibrous cap was thinnest on the proximal side of the plaque, compared with the distal side. These results thus agree with the findings of Lovett (Lovett and Rothwell, 2003), and principal stress levels may be the cause of the asymmetrical longitudinal distribution of plaque rupture with the majority occurring proximally to the plaque.

Previous studies have used principal stress levels in excess of 300 kPa to be predictive of plaques at high risk of rupture (Cheng et al., 1993; Li et al., 2006b; Li et al., 2007). However, the choice of material model and parameters may substantially affect simulated stress levels (Li et al., 2006a). Care should thus be taken comparing absolute stress levels across different simulations employing different material models, and the choice of an absolute level at which the plaques are considered to be at risk of rupture may be problematic.

Currently, state-of-the-art MRI scans employ typical in plane spatial resolutions of 0.5 – 0.6 mm (Yuan and Kerwin, 2004; Crowe et al., 2005). Stress levels increased dramatically with decreasing fibrous cap widths, particularly below 0.2 mm. Increasing spatial resolution to enable visualization of very thin fibrous caps could thus prove of vital importance. Moving towards scanners with higher field strengths (Yarnykh et al., 2006) or switching from 2D to 3D acquisitions (Koktzoglou and Li, 2007) may facilitate this.

5. Conclusion

The new technique of obtaining longitudinal 2D computational models of the carotid artery was systematically investigated using idealized carotid bifurcation geometry with variables thought to be linked to risk of carotid plaque rupture; degree of stenosis, fibrous cap thickness, and lipid core size, all of which affected stress levels severely. Numerous histopathological studies have indicated lipid pool size and fibrous cap thickness to be key determinants of plaque vulnerability. Principal stresses may be of additional merit, since this parameter combines effects of fibrous cap thickness, lipid pool size, degree of stenosis, and blood pressure into a single comprehensive risk assessment marker. With the advent of fast computational techniques for obtaining in-vivo stress levels, assessing risk of plaque rupture using peak principal stress levels is enabled which may lead to improved reliability of carotid risk assessment in the future.

6. References

Versluis, A., Bank, A.J., Douglas, W.H., 2006. Fatigue and plaque rupture in myocardial infarction. *Journal of Biomechanics* 39, 339-347

Antheunis, V Alan, JB William, HD, (2006). Fatigue and plaque rupture in myocardial infarction. pp. 339-347.

Banks, J. Bressloff, N.W., 2007. Turbulence modeling in three-dimensional stenosed arterial bifurcations. *Journal of Biomechanical Engineering* 129, 40-50.

Bassiouny, H.S. Sakaguchi, Y. et al., 1997. Juxtalumenal location of plaque necrosis and neoformation in symptomatic carotid stenosis. *J.Vasc.Surg*. 26, 585-594.

Botnar, R.M. Stuber, M. et al., 2001. Magnetic resonance coronary lumen and vessel wall imaging. *Rays* 26, 291-303.

Cai, J.M. Hatsukami, T.S. et al., 2002. Classification of human carotid atherosclerotic lesions with in vivo multicontrast magnetic resonance imaging. *Circulation* 106, 1368-1373.

Carr, S. Farb, A. et al., 1996. Atherosclerotic plaque rupture in symptomatic carotid artery stenosis, , . *Journal of Vascular Surgery* 23**,** 755-766.

Casscells, W. Naghavi, M. et al., 2003. Vulnerable atherosclerotic plaque: a multifocal disease. *Circulation* 107**,** 2072-2075.

Chau, A.H. Chan, R.C. et al., 2004. Mechanical analysis of atherosclerotic plaques based on optical coherence tomography. *Ann.Biomed.Eng* 32**,** 1494-1503.

Chen, C.H. Ting, C.T. et al., 1996. Validation of Carotid Artery Tonometry as a Means of Estimating Augmentation Index of Ascending Aortic Pressure. *Hypertension* 27**,** 168-175.

Cheng, G.C. Loree, H.M. et al., 1993. Distribution of circumferential stress in ruptured and stable atherosclerotic lesions. A structural analysis with histopathological correlation. *Circulation* 87**,** 1179-1187.

Chu, B. Kampschulte, A. et al., 2004. Hemorrhage in the atherosclerotic carotid plaque: a high-resolution MRI study. *Stroke* 35**,** 1079-1084.

Claudon, M. Winninger, D. et al., 2001. Power Doppler US: Evaluation of the Morphology of Stenoses with a Flow Phantom. *Radiology* 218**,** 109-117.

Clevert, D.A. Johnson, T. et al., 2007. Color Doppler, power Doppler and B-flow ultrasound in the assessment of ICA stenosis: Comparison with 64-MD-CT angiography. *European Radiology* 17**,** 2149-2159.

Clevert, D.A. Johnson, T. et al., 2006. High-grade stenoses of the internal carotid artery: Comparison of high-resolution contrast enhanced 3D MRA, duplex sonography and power Doppler imaging. *European Journal of Radiology* 60**,** 379-386.

COMSOL AB, (2005). Comsol Multiphysics: Structural Mechanics Module. *COMSOL AB*, Stockholm, Sweden.

Crowe, L.A. Keegan, J. et al., 2005. 3D volume-selective turbo spin echo for carotid artery wall imaging with navigator detection of swallowing. *J Magn Reson.Imaging* 22**,** 583-588.

Dart, A.M. Kingwell, B.A., 2001. Pulse pressure--a review of mechanisms and clinical relevance. *Journal of the American College of Cardiology* 37**,** 975-984.

Draney, M.T. Herfkens, R.J. et al., 2002. Quantification of vessel wall cyclic strain using cine phase contrast magnetic resonance imaging. *Ann.Biomed.Eng* 30**,** 1033-1045.

ECST, 1991. MRC European Carotid Surgery Trial: interim results for symptomatic patients with severe (70-99%) or with mild (0-29%) carotid stenosis. *European Carotid Surgery Trialists' Collaborative Group. Lancet* 337**,** 1235-1243.

ECST, 1998. Randomised trial of endarterectomy for recently symptomatic carotid stenosis: final results of the MRC European Carotid Surgery Trial (ECST). *Lancet* 351**,** 1379-1387.

Falk, E., 2006. Pathogenesis of atherosclerosis. *Journal of the American College of Cardiology* 47**,** C7-12.

Falk, E., 1992. Why do plaques rupture? *Circulation* 86**,** III30-III42.

Falk, E. Shah, P.K. et al., 1995. Coronary Plaque Disruption. *Circulation* 92**,** 657-671.

Firmin, D.N. Nayler, G.L. et al., 1990. The application of phase shifts in NMR for flow measurement. *Magn Reson.Med.* 14**,** 230-241.

Frayne, R. Steinman, D.A. et al., 1995. Accuracy of MR phase contrast velocity measurements for unsteady flow. *J Magn Reson.Imaging* 5**,** 428-431.

Glagov, S. Weisenberg, E. et al., 1987. Compensatory enlargement of human atherosclerotic coronary arteries. *New England Journal of Medicine* 316**,** 1371-1375.

Glagov, S. Zarins, C. et al., 1988. Hemodynamics and atherosclerosis. Insights and perspectives gained from studies of human arteries. *Arch Pathol Lab Med* 112**,** 1018-1031.

Gronholdt, M.L. Dalager-Pedersen, S. et al., 1998. Coronary atherosclerosis: determinants of plaque rupture. *Eur.Heart J.* 19 Suppl C**,** C24-C29.

Halliday, A. Mansfield, A. et al., 2004. Prevention of disabling and fatal strokes by successful carotid endarterectomy in patients without recent neurological symptoms: randomised controlled trial. *Lancet* 363**,** 1491-1502.

Hatsukami, T.S. Ross, R. et al., 2000. Visualization of fibrous cap thickness and rupture in human atherosclerotic carotid plaque in vivo with high-resolution magnetic resonance imaging. *Circulation* 102**,** 959-964.

Hayes, C.E. Mathis, C.M. et al., 1996. Surface coil phased arrays for high-resolution imaging of the carotid arteries. *J.Magn Reson.Imaging* 6**,** 109-112.

Holzapfel, G.A. Sommer, G. et al., 2004. Anisotropic mechanical properties of tissue components in human atherosclerotic plaques. *J Biomech Eng* 126**,** 657-665.

Huang, D. Swanson, E.A. et al., 1991. Optical coherence tomography. *Science* 254**,** 1178-1181.

Huang, H. Virmani, R. et al., 2001. The Impact of Calcification on the Biomechanical Stability of Atherosclerotic Plaques. *Circulation* 103**,** 1051-1056.

Imoto, K. Hiro, T. et al., 2005. Longitudinal Structural Determinants of Atherosclerotic Plaque Vulnerability: A Computational Analysis of Stress Distribution Using Vessel Models and Three-Dimensional Intravascular Ultrasound Imaging. *Journal of the American College of Cardiology* j.

Jin, S. Yang, Y. et al., 2004. Flow patterns and wall shear stress distributions at atherosclerotic-prone sites in a human left coronary artery--an exploration using combined methods of CT and computational fluid dynamics. *Conf.Proc.IEEE Eng Med Biol Soc.* 5**,** 3789-3791.

Kaazempur-Mofrad, M.R. Isasi, A.G. et al., 2004. Characterization of the atherosclerotic carotid bifurcation using MRI, finite element modeling, and histology. *Ann Biomed Eng* 32**,** 932-946.

Kario, K. Pickering, T.G. et al., 2003. Morning Surge in Blood Pressure as a Predictor of Silent and Clinical Cerebrovascular Disease in Elderly Hypertensives: A Prospective Study. *Circulation* 107**,** 1401-1406.

Koktzoglou, I. Li, D., 2007. Submillimeter isotropic resolution carotid wall MRI with swallowing compensation: imaging results and semiautomated wall morphometry. *J Magn Reson.Imaging* 25**,** 815-823.

Lee, S.W. Steinman, D.A., 2007. On the relative importance of rheology for image-based CFD models of the carotid bifurcation. *J.Biomech.Eng* 129**,** 273-278.

Li, Z.Y. Howarth, S. et al., 2006a. Stress analysis of carotid plaque rupture based on in vivo high resolution MRI. *Journal of Biomechanics* 39**,** 2611-2622.

Li, Z.Y. Howarth, S.P.S. et al., 2006b. How Critical Is Fibrous Cap Thickness to Carotid Plaque Stability?: A Flow-Plaque Interaction Model. *Stroke* 37**,** 1195-1199.

Li, Z.Y. Howarth, S.P.S. et al., 2007. Structural analysis and magnetic resonance imaging predict plaque vulnerability: A study comparing symptomatic and asymptomatic individuals. *Journal of Vascular Surgery* 45**,** 768-775.

Liu, F. Xu, D. et al., 2006. Automated in vivo segmentation of carotid plaque MRI with Morphology-Enhanced probability maps. *Magnetic Resonance in Medicine* 55, 659-668.

Loree, H.M. Kamm, R.D. et al., 1992. Effects of fibrous cap thickness on peak circumferential stress in model atherosclerotic vessels. *Circulation Research* 71, 850-858.

Lovett, J.K. Rothwell, P.M., 2003. Site of carotid plaque ulceration in relation to direction of blood flow: An angiographic and pathological study. *Cerebrovascular Diseases* 16, 369-375.

Lui, E.Y.L. Steinman, A.H. et al., 2005. Human factors as a source of error in peak Doppler velocity measurement. *Journal of Vascular Surgery* 42, 972.

McDonnell, C.H., III Herfkens, R.J. et al., 1994. Magnetic resonance imaging and measurement of blood flow. *West J Med*. 160, 237-242.

Mead, G.E. Lewis, S.C. et al., 2000. Variability in Doppler ultrasound influences referral of patients for carotid surgery. *European Journal of Ultrasound* 12, 137-143.

Metafratzi, Z.M. Efremidis, S.C. et al., 2002. The clinical significance of aortic compliance and its assessment with magnetic resonance imaging. *Journal of Cardiovascular Magnetic Resonance* 4, 481-491.

Mitsumori, L.M. Hatsukami, T.S. et al., 2003. In vivo accuracy of multisequence MR imaging for identifying unstable fibrous caps in advanced human carotid plaques. *J.Magn Reson.Imaging* 17, 410-420.

Naghavi, M. Libby, P. et al., 2003. From Vulnerable Plaque to Vulnerable Patient: A Call for New Definitions and Risk Assessment Strategies: Part I. *Circulation* 108, 1664-1672.

NASCET, 1991. Beneficial effect of carotid endarterectomy in symptomatic patients with high-grade carotid stenosis. North American Symptomatic Carotid Endarterectomy Trial Collaborators. *New England Journal of Medicine* 325, 445-453.

Nederkoorn, P.J. van der, G.Y. et al., 2003. Duplex ultrasound and magnetic resonance angiography compared with digital subtraction angiography in carotid artery stenosis: a systematic review. *Stroke* 34, 1324-1332.

Nighoghossian, N. Derex, L. et al., 2005. The Vulnerable Carotid Artery Plaque: Current Imaging Methods and New Perspectives. *Stroke* 36, 2764-2772.

Pasterkamp, G. Smits, P.C., 2002. Imaging of atherosclerosis. Remodelling of coronary arteries. *J.Cardiovasc.Risk* 9, 229-235.

Perktold, K. Rappitsch, G., 1995. Computer simulation of local blood flow and vessel mechanics in a compliant carotid artery bifurcation model. *J.Biomech.* 28, 845-856.

Piegl, L., Tiller, W., (1997). The NURBS Book. Springer-Verlag, New York, NY.

Ramaswamy, S.D. Vigmostad, S.C. et al., 2006. Comparison of left anterior descending coronary artery hemodynamics before and after angioplasty. *J Biomech Eng* 128, 40-48.

Redgrave, J.N.E. Lovett, J.K. et al., 2006. Histological Assessment of 526 Symptomatic Carotid Plaques in Relation to the Nature and Timing of Ischemic Symptoms: The Oxford Plaque Study. *Circulation* 113, 2320-2328.

Roemer, P.B. Edelstein, W.A. et al., 1990. The NMR phased array. *Magn Reson.Med.* 16, 192-225.

Rosamond, W. Flegal, K. et al., 2007. Heart Disease and Stroke Statistics--2007 Update: A Report From the American Heart Association Statistics Committee and Stroke Statistics Subcommittee. Circulation 115, e69-171.

Rothwell, P.M. Eliasziw, M. et al., 2003a. Analysis of pooled data from the randomised controlled trials of endarterectomy for symptomatic carotid stenosis. *Lancet* 361, 107-116.

Rothwell, P.M. Howard, S.C. et al., 2003b. Relationship Between Blood Pressure and Stroke Risk in Patients With Symptomatic Carotid Occlusive Disease. *Stroke* 34, 2583-2590.

Shinnar, M. Fallon, J.T. et al., 1999. The diagnostic accuracy of ex vivo MRI for human atherosclerotic plaque characterization. *Arteriosclerosis, Thrombosis, and Vascular Biology* 19, 2756-2761.

Sipahi, I. Tuzcu, E.M. et al., 2007. Does the extent and direction of arterial remodeling predict subsequent progression of coronary atherosclerosis? A serial intravascular ultrasound study. *Heart hrt.*

Small, D.M. Shipley, G.G., 1974. Physical-chemical basis of lipid deposition in atherosclerosis. *Science* 185, 222-229.

Staessen, J.A. Fagard, R. et al., 1997. Randomised double-blind comparison of placebo and active treatment for older patients with isolated systolic hypertension. *The Lancet* 350, 757-764.

Stary, H.C. Chandler, A.B. et al., 1995. A Definition of Advanced Types of Atherosclerotic Lesions and a Histological Classification of Atherosclerosis : A *Report From the Committee on Vascular Lesions of the Council on Arteriosclerosis, American Heart Association. Arteriosclerosis, Thrombosis, and Vascular Biology* 15, 1512-1531.

Steinman, D.A., 2002. Image-based computational fluid dynamics modeling in realistic arterial geometries. *Ann.Biomed.Eng* 30, 483-497.

Tang, D. Yang, C. et al., 2004. 3D MRI-based multicomponent FSI models for atherosclerotic plaques. *Annals of Biomedical Engineering* 32, 947-960.

Titi, M. George, C. et al., 2007. Comparison of carotid Doppler ultrasound and computerised tomographic angiography in the evaluation of carotid artery stenosis. *Surgeon.* 5, 132-136.

Tola, M. Yurdakul, M., 2006. Effect of Doppler Angle in Diagnosis of Internal Carotid Artery Stenosis. *Journal of Ultrasound in Medicine* 25, 1187-1192.

Virmani, R. Kolodgie, F.D. et al., 2000. Lessons from sudden coronary death: a comprehensive morphological classification scheme for atherosclerotic lesions. *Arterioscler.Thromb.Vasc.Biol.* 20, 1262-1275.

Virmani, R. Ladich, E.R. et al., 2006. Histopathology of carotid atherosclerotic disease. *Neurosurgery* 59, S219-S227.

Wentzel, J.J. Gijsen, F.J.H. et al., 2003. Shear stress, vascular remodeling and neointimal formation. *Journal of Biomechanics* 36, 681-688.

WHO and CDC, (2004). T*he Atlas of Heart Disease and Stroke*.

Yabushita, H. Bouma, B.E. et al., 2002. Characterization of Human Atherosclerosis by Optical Coherence Tomography. *Circulation* 106, 1640-1645.

Yarnykh, V.L. Terashima, M. et al., 2006. Multicontrast black-blood MRI of carotid arteries: comparison between 1.5 and 3 tesla magnetic field strengths. *Journal of Magnetic Resonance Imaging* 23, 691-698.

Yarnykh, V. L., Yuan, C., (2003). High-Resolution Multi-Contrast MRI of the Carotid Artery Wall for Evaluation of Atherosclerotic Plaques. *Current Protocols in Magnetic Resonance Imaging*. John Wiley & Sons.

Yuan, C. Beach, K.W. et al., 1998. Measurement of atherosclerotic carotid plaque size in vivo using high resolution magnetic resonance imaging. *Circulation* 98**,** 2666-2671.

Yuan, C. Kerwin, W.S., 2004. MRI of atherosclerosis. *Journal of Magnetic Resonance Imaging* 19**,** 710-719.

Yuan, C. Lin, E. et al., 1999. Closed contour edge detection of blood vessel lumen and outer wall boundaries in black-blood MR images. *Magn Reson.Imaging* 17**,** 257-266.

Yuan, C. Mitsumori, L.M. et al., 2001. In vivo accuracy of multispectral magnetic resonance imaging for identifying lipid-rich necrotic cores and intraplaque hemorrhage in advanced human carotid plaques. *Circulation* 104**,** 2051-2056.

Yuan, C. Petty, C. et al., 1997. In vitro and in situ magnetic resonance imaging signal features of atherosclerotic plaque-associated lipids. *Arterioscler.Thromb.Vasc.Biol.* 17**,** 1496-1503.

Yuan, C. Zhang, S.X. et al., 2002. Identification of fibrous cap rupture with magnetic resonance imaging is highly associated with recent transient ischemic attack or stroke. *Circulation* 105**,** 181-185.

Yusuf, S. Reddy, S. et al., 2001. Global Burden of Cardiovascular Diseases: Part I: General Considerations, the Epidemiologic Transition, Risk Factors, and Impact of Urbanization. *Circulation* 104**,** 2746-2753.

Zhao, S.Z. Ariff, B. et al., 2002. Inter-individual variations in wall shear stress and mechanical stress distributions at the carotid artery bifurcation of healthy humans. *Journal of Biomechanics* 35**,** 1367-1377.

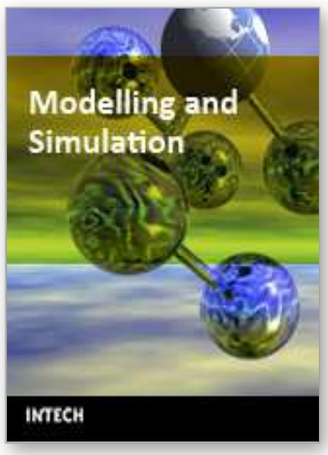

Modelling and Simulation

Edited by Giuseppe Petrone and Giuliano Cammarata

ISBN 978-3-902613-25-7
Hard cover, 688 pages
Publisher I-Tech Education and Publishing
Published online 01, June, 2008
Published in print edition June, 2008

This book collects original and innovative research studies concerning modeling and simulation of physical systems in a very wide range of applications, encompassing micro-electro-mechanical systems, measurement instrumentations, catalytic reactors, biomechanical applications, biological and chemical sensors, magnetosensitive materials, silicon photonic devices, electronic devices, optical fibers, electro-microfluidic systems, composite materials, fuel cells, indoor air-conditioning systems, active magnetic levitation systems and more. Some of the most recent numerical techniques, as well as some of the software among the most accurate and sophisticated in treating complex systems, are applied in order to exhaustively contribute in knowledge advances.

InTech Europe
University Campus STeP Ri
Slavka Krautzeka 83/A
51000 Rijeka, Croatia
Phone: +385 (51) 770 447
Fax: +385 (51) 686 166
www.intechopen.com

InTech China
Unit 405, Office Block, Hotel Equatorial Shanghai
No.65, Yan An Road (West), Shanghai, 200040, China
中国上海市延安西路65号上海国际贵都大饭店办公楼405单元
Phone: +86-21-62489820
Fax: +86-21-62489821

IntechOpen